Optimization of the Compton camera for measuring prompt gamma rays in boron neutron capture therapy

CrossMark

Chun-hui Gong[a,b], Xiao-bin Tang[a,c,*], Di-yun Shu[a], Hai-yan Yu[a], Chang-ran Geng[a]

[a] Department of Nuclear Science and Engineering, Nanjing University of Aeronautics and Astronautics, Nanjing, China
[b] National Institute of Nuclear Physics, INFN, Section of Pavia, Italy
[c] Collaborative Innovation Center of Radiation Medicine of Jiangsu Higher Education Institutions, Nanjing, China

ARTICLE INFO

ABSTRACT

Optimization of the Compton camera for measuring prompt gamma rays (0.478 MeV) emitted during boron neutron capture therapy (BNCT) was performed with Geant4. The parameters of the Compton camera were determined as follows: 3 cm thick – 10 cm wide scatter detector (Silicon), 10 cm thick – 10 cm wide absorber detector (Germanium), and 1 cm distance between the scatter and absorber detectors. For a typical brain tumor treatment, the overall detection efficiency of the optimized Compton camera was approximately 0.1425% using the Snyder's head phantom with a sphere tumor (4 cm diameter and ~1 cm depth).

1. Introduction

Radiation therapy (RT) has been a valuable treatment method for cancer. The principle of RT is to deliver most of the doses to the tumor while minimizing the dose to the healthy tissues. As a special type of RT, BNCT (Bortolussi et al., 2014; Chao et al., 2016; Hang et al., 2016; Sauerwein, 2012) is considered as a binary radiotherapy that combines the targeting feature of a novel boron-containing material. Fig. 1 illustrates the process during BNCT. BNCT uses the nuclear capture reaction of the thermal neutron and ^{10}B. The secondary charged particles (α and ^7Li) have a finite range, which is on the cellular scale. Therefore, the radiation damage only occurs in the targeted cell.

However, one of the most important concerns of BNCT is determining the exact position of boron (i.e., the location of boron neutron capture reaction), and obtaining a real-time image of the location being treated has not been possible to-date. Therefore, new methods of obtaining an image of the treatment region are being developed. The characteristic prompt gamma rays emitted have been used to address this issue because they are emitted in-situ during the neutron capture interaction. Several researchers (Hales et al., 2014; Ishikawa et al., 2000; Kobayashi et al., 2000; Minsky et al., 2011; Murata et al., 2011; Rosenschöld et al., 2006; Verbakel and Stecher-Rasmussen, 2001; Yoon et al., 2014) recently began to investigate the use of the single-photon emission computed tomography (SPECT) imaging as a means of achieving the real-time image of the treatment region. However, SPECT cameras rely on two-dimensional (2D) collimation of the gamma rays to produce images, which limits their sensitivity and spatial resolution.

The Compton camera is a possible method for prompt gamma ray detection and overcomes the limitations of the SPECT imaging. The Compton camera localizes the position where the gamma ray is emitted by analyzing the kinematics of the Compton scattering. The Compton camera consists of at least two sensitive detectors, i.e., scatter detector and absorber detector, to score the position and energy loss of the Compton reaction. Several research groups (Lee et al., 2015; Stockhausen, 2012) proposed the application of the Compton camera for the measurement of the prompt gamma rays during BNCT. Stockhausen (2012) evaluated the feasibility of using the Compton camera in BNCT. However, to the best knowledge of the authors, no optimization study was found for the specific application. This fact limits the efficiency of the Compton camera in BNCT. Therefore, a study on the theoretical design of the Compton camera for its application in BNCT is required, i.e. optimizing its overall detection efficiency (i.e., effective counts) particularly for 0.478 MeV prompt gamma rays emitted during BNCT. The condition of the clinical BNCT environment for the Compton camera is complex and challenging in terms of neutron contamination, scatters, and algorithms for reconstruction (Peterson et al., 2010) and will be further researched in detail in future studies; thus, it is not in the scope of this current study.

The objective of this current study was to develop an optimal Compton camera specifically designed for measuring the characteristic prompt gamma rays emitted from the tissue during BNCT. The Compton camera geometry was optimized with Monte Carlo calculations. We basically used similar procedure as the Peterson study (Peterson et al., 2010), which was dedicated to prompt gamma camera design for

* Corresponding author at: Nanjing University of Aeronautics and Astronautics, China.
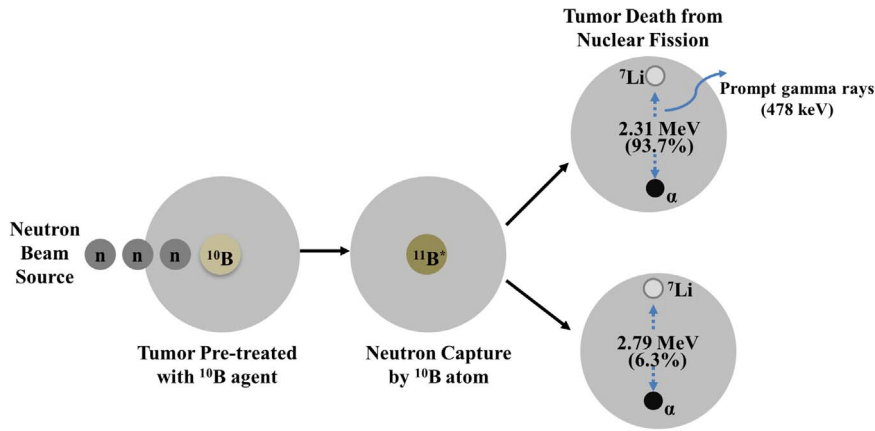 *E-mail address:* tangxiaobin@nuaa.edu.cn (X.-b. Tang).

Fig. 1. Nuclear reactions of BNCT. The ^{10}B captures a neutron and then ^{11}B disintegrates in 93.7% into an α particle and an excited ^{7}Li nucleus, releasing a 0.478 MeV prompt gamma ray when it de-excited to its ground state.

proton therapy. The optimization was based on the optimal detection efficiency (i.e., effective count) of detectors with an isotropic gamma source. The thickness and the lateral width of the two detectors, i.e., one scatter detector and one absorber detector, as well as the distance between the two detectors, were determined by the effective counts of the Compton camera. Then, the neutron source was used to irradiate the Snyder's head phantom with a tumor, and the total number of prompt gamma rays detected was recorded in the Compton camera. These steps were performed to determine the feasibility of using the optimized Compton camera to measure the prompt gamma rays for BNCT and provided an overall detection efficiency in measuring prompt gamma rays emitted from the tissue during BNCT.

2. Materials and methods

2.1. Principle of a Compton camera

In a Compton camera system, the gamma rays emitted from a source placed in front of the scatter detector are scattered by electrons in the scatter detector, depositing a fraction of its energy before getting fully absorbed in the absorber detector. Under the circumstance where the deposited energies and interaction positions in both detectors are measured, the resulting angular distribution may be estimated by a cone with a central axis co-linear to the first and second interactions, and an angle, θ, computed from the following Compton equation:

$$cos\theta = 1 - m_e c^2 (1/E_2 - 1/E_\gamma) \qquad (1)$$

where E_γ is the initial gamma energy, $m_e c^2$ is the electron rest energy, and E_1 and E_2 are the energies deposited at P_1 and P_2, respectively (Fig. 2). This event is denoted as a "true event". The apex of the Compton cone is P_1, the axis of the cone is the line P_1P_2, and the half-angle of the cone is θ. The gamma ray emission points can be reconstructed by overlapping the cones from many interactions. The principle of the Compton camera is illustrated in Fig. 2.

2.2. Monte Carlo simulations

The simulations were performed with Geant4 toolkit (Geng et al., 2016; Guan et al., 2015; Wright, 2002), which is a Monte Carlo toolkit, composed of C++ libraries. The *G4PenelopeComptonModel* was utilized to accurately simulate the Compton scattering process. The process implementation has been validated by several studies, and it has been validated with many external reference libraries (Cirrone et al., 2010; Weidenspointner et al., 2013). The Compton camera in this study was composed of a silicon detector (scatter detector) and a germanium detector (absorber detector). Silicon detector was sleeted for the potential for electron track Compton imaging (Thirolf et al., 2016),
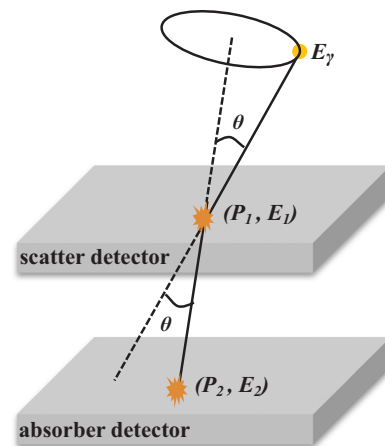

Fig. 2. The principle of the Compton camera. It consists of a scatter detector and an absorber detector. The Compton cone is constructed by the interaction positions and energies.
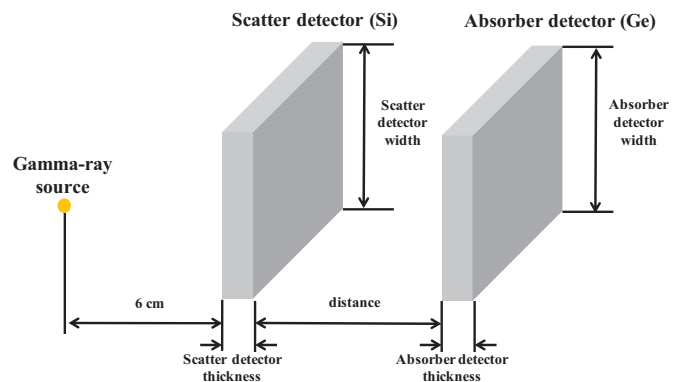

Fig. 3. The setup of the Geant4 simulation. A gamma point source is suited on the center axis of the Compton camera at a distance of 6 cm from the scatter detector.

which would increase the reconstruction efficiency. Germanium detector was chosen for its good energy resolution. The detectors, arranged in parallel-plane geometry, were modeled in Geant4 as shown in Fig. 3. An isotropic point source with an energy of 0.478 MeV was used in the Monte Carlo simulation to study the overall detection efficiency of the prompt gamma rays in BNCT. It was positioned at the center of the Compton camera field of view at a distance of 6 cm from the scatter detector. The thickness and lateral width of the two detectors, as well as the distance between the two detectors were studied as the variables for the optimization.
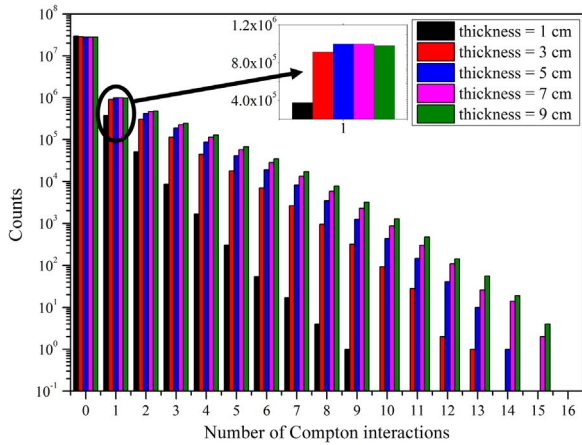
Fig. 4. The distribution of the number of Compton interactions in the scatter detector with the thickness of the scatter detector at 1 cm, 3 cm, 5 cm, 7 cm, and 9 cm.

3. Results and discussion

3.1. The thickness of scatter detector

Its lateral width was set at a fixed value of 10 cm to study the relationship between the detector efficiency and its thickness. The simulations were run to obtain a statistical error lower than 3% with 3×10^7 particles. Fig. 4 shows the distribution of the number of Compton interactions in the scatter detector (Si) for 0.478 MeV gamma rays. Zero means that the gamma ray does not enter the scatter detector. One stands for a single Compton interaction in the scatter detector, considering both the case with energy escape and the case without escape. The Compton interaction without energy escape means that the recoil electron deposits all its energy in the scatter detector. Numbers greater than one represent the multiple Compton interactions in the scatter detector.

Based on the principle of the Compton Camera, only the single Compton interaction in the scatter detector can be used in the Compton cone reconstruction. Therefore, the counts of single Compton interactions were considered in the optimization of the scatter detector. The detection efficiency of the scatter detector, ε_1, can be defined as follows:

$$\varepsilon_1 = N_{single\_Compton\_interaction}/N_{prompt\_gamma\_rays} \qquad (2)$$

where $N_{single\_Compton\_interaction}$ is the number of single Compton interactions in a scatter detector, and $N_{prompt\_gamma\_rays}$ is the number of emitted prompt gamma rays. Fig. 5 shows the relationship between the detection efficiency of single Compton interactions and the thickness of
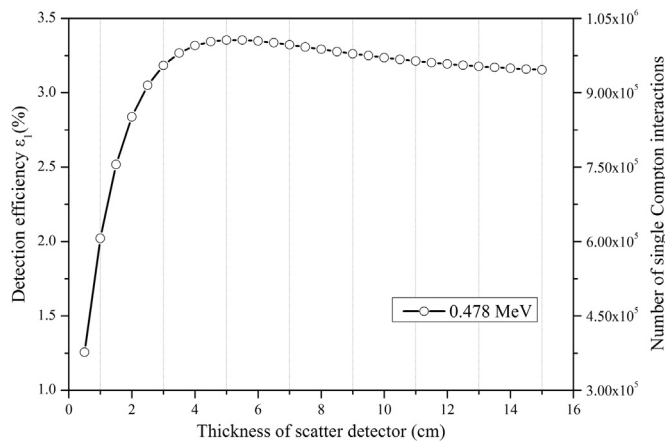

Fig. 5. Detection efficiency results (left axis) of a single Compton interaction when the thickness of the scatter detector range from 0.5 to 15 cm. On the right axis is the number of single Compton interactions detected from 3×10^7 photons.
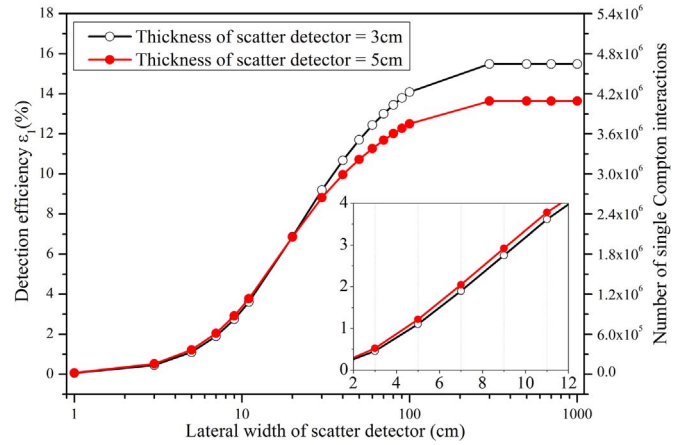

Fig. 6. Detection efficiency results (left axis) for single Compton interactions when the lateral width of the scatter detector ranges from 1 cm to 1000 cm. On the right axis is the number of single Compton interactions detected from 3×10^7 photons.

the scatter detector. The detection efficiency is given by the number of single Compton interactions shown in the right-hand scale in Fig. 5.

The detection efficiency of the scatter detector increased as the scatter detector thickness increased initially, and decreased afterward. The detection efficiency of the scatter detector reached the maximum value when the thickness of the scatter detector was around 3–5 cm. The results can be attributed to the single Compton interactions in the scatter detector that initially increased with an increasing thickness; as the thickness continues to increase, the multiple Compton interactions become more prevalent, which caused a decrease in the number of single Compton interactions in the scatter detector. The 3 cm and 5 cm were considered as the optimized thickness that can be further discussed in combination with the lateral width for practical applications.

3.2. The lateral width of scatter detector

The thickness was set at a fixed value of 3 cm and 5 cm to study the relationship between the detector efficiency and its lateral width. Fig. 6 shows the relationship between the detection efficiency of single Compton interactions and the lateral width of the scatter detector. The detection efficiency of single Compton interactions increased as the lateral width of the scatter detector increased initially, reached the maximum value at approximately 300 cm, and then remained almost unchanged. This behavior can be explained by the influence of the solid angle (Ω). For the isotropic gamma source, the efficiency of the gamma ray entering the scatter detector was dependent on the lateral width of the detector but independent of the detector thickness and gamma ray energy. The efficiency follows the solid angle (Ω) relationship for a square plane detector as given by:

$$\Omega = \arcsin[\omega_1^2/(d^2 + \omega_1^2)] \qquad (3)$$

where d is the distance from the source to the scatter detector, and ω_1 is the lateral width of the scatter detector. The results in Fig. 6 show that the counts of single Compton interactions increased with ω_1 over the range of thickness studied in Section 3.1.

The detection efficiency at 3 cm is almost equal to that at 5 cm, whereas the lateral width of the scatter detector ranged from 1 cm to 20 cm. The details can be seen from the enlarged figure in Fig. 6. Therefore, the optimal thickness of the scatter detector was 3 cm.

The maximum value of the detection efficiency occurred in the impractical lateral width of the scatter detector (> 300 cm). A more practical value, 10 cm, was chosen for the lateral width of the scatter detector. Hence, the optimal dimension of the scatter detector was a thickness of 3 cm and a lateral width of 10 cm.
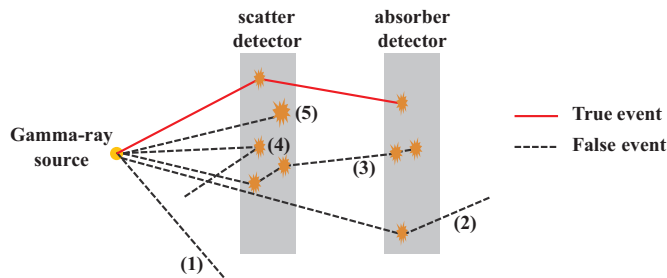
Fig. 7. The conditions of Compton camera.

3.3. The thickness of absorber detector

5 cases have been defined ("false events") to explain five different conditions in which the gamma event cannot be considered in the efficiency calculation, as shown in Fig. 7. In particular, the gamma rays escape in all directions from the source, causing a fraction of the gamma rays to miss the scatter detector (false event #1). Some of the incident gamma rays scatter out of the absorber detector (false event #2). A part of the incident gamma rays, which interacts in multiple points in one of the detectors (i.e. multiple events), is discarded because only single interactions were considered (false event #3). A section of the incident gamma rays is lost because the scatter photons do not enter the absorber detector (false event #4). A portion of the incident gamma rays gets lost because the scatter photons are absorbed fully by the scatter detector (false event #5). In Fig. 7, the detection efficiency is expected to be lower due to the thickness of the absorber detector, if compare to the scatter detector, because of the occurrence of false events #4 and #5. The overall detection efficiency, ε_2, can be calculated as follows:

$$\varepsilon_2 = N_{\text{true\_events}}/N_{\text{prompt\_gamma\_rays}} \tag{4}$$

where $N_{\text{true\_events}}$ is the number of true events, and $N_{\text{prompt\_gamma\_rays}}$ is the number of emitted prompt gamma rays.

Fig. 8 shows the relationship between the overall detection efficiency of true events and the thickness of the absorber detector, whereas the distances of the detectors are 1 cm, 3 cm, and 5 cm. Its lateral width was set at a fixed value of 10 cm. Regardless of the distance between the two detectors, the overall detection efficiency of the true events increased as the thickness of the absorber detector increased initially, reached the maximum value at 10 cm, and then remained almost unchanged. This result is attributed to the increasing thickness of the absorber detector, causing more usable interactions. Hence, the practical thickness value of the absorber detector was 10 cm.
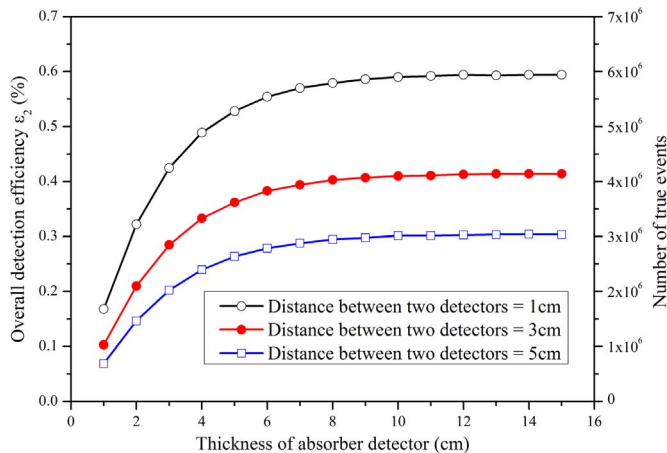

Fig. 8. Overall detection efficiency (left axis) of true events when the thickness of the absorber detector ranges from 1 cm to 15 cm. On the right axis is the number of true events detected from 1×10^8 photons.
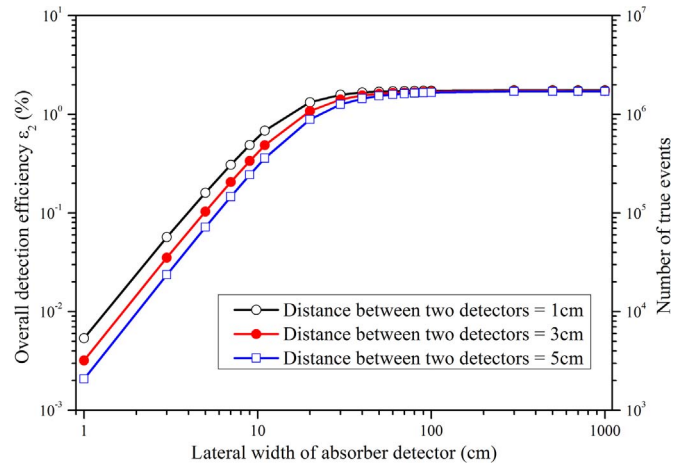

Fig. 9. Overall detection efficiency (left axis) of the true events when the lateral width of the absorber detector ranges from 1 cm to 1000 cm. On the right axis is the number of the true events detected from 1×10^8 photons.

3.4. The lateral width of absorber detector

The thickness of the absorber detector was fixed at 10 cm to study the relationship between the detector efficiency and the lateral width of the absorber detector. The lateral width of the absorber detector affected the number of single, scattered gamma rays from the scatter detector that entered the absorber detector. Fig. 9 shows the relationship between the overall detection efficiency of the true events and the lateral width of the absorber detector. The thickness and lateral width of the scatter detector and the thickness of the absorber detector were set at 3 cm, 10 cm, and 10 cm, respectively.

The solid angle formula does not apply in this case because of the attenuation of the scatter detector. The overall detection efficiency was increased as the lateral width of the absorber detector increased and reached a saturation value of 50 cm. However, a width of 10 cm was chosen for the absorber detector because of the limitations in the current manufacturing capabilities with high purity germanium detectors (Peterson et al., 2010). Therefore, the optimal dimensions of the absorber detector are 10 cm thickness and 10 cm width.

3.5. The distance between scatter detector and absorber detector

The distance between the two detectors is also an important parameter of the Compton camera, which determines its maximum overall detection efficiency ε_2. A study of the relationship between the detector efficiency and the distance between the two detectors used the following parameters. The thickness and the width of the scatter detector were set at 3 cm and 10 cm, respectively, whereas the thickness and the width of the absorber detector were set at 10 cm and 10 cm, respectively. Fig. 10 shows the overall detection efficiency of the true events and the true event counts changed with the different distances between the two detectors.

Reducing the distance between the two detectors produced an increase in the true event counts resulting in an increase detection efficiency of true events, which is also the overall Compton camera efficiency. The overall detection efficiency ε_2 ranged from 0.16% to 0.59%, whereas the distance between the two detectors was set from 10 cm to 1 cm. The value of the distance between detectors that optimizes the efficiency is 1 cm. These parameters led to a final optimized Compton camera for BNCT with detector dimensions of 3 cm thick – 10 cm wide for the scatter detector, 10 cm thick – 10 cm wide for the absorber detector, and a 1 cm distance between the two detectors.
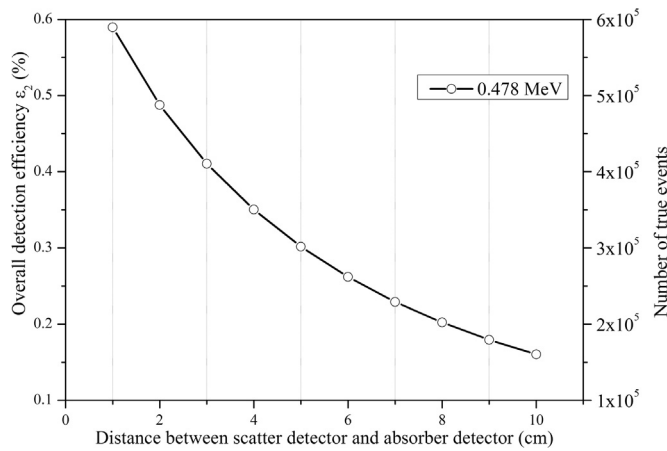
Fig. 10. Overall detection efficiency (left axis) of the true events when the distances between the two detectors ranges from 1 cm to 10 cm. On the right axis is the number of true events detected from 1×10^8 photons.

3.6. Phantom study with BNCT

The neutron source was used to irradiate the Snyder's head phantom with a tumor to calculate the overall detection efficiency of the optimized Compton camera during BNCT to further evaluate the performance of this optimized Compton camera. This phantom contains brain, skull, and skin, which are geometrically described by the following formulas:

$$Brain : (x/6)^2 + (y/9)^2 + ((z-1)/6.5)^2 = 1 \quad (5)$$

$$Skull: (x/6.8)^2 + (y/9.8)^2 + (z/8.3)^2 = 1 \quad (6)$$

$$Skin : (x/7.3)^2 + (y/10.3)^2 + (z/8.8)^2 = 1 \quad (7)$$

A spherical tumor with ^{10}B was considered in the depth of ~1 cm, and the diameter was set at 4 cm. ^{10}B concentration in the tumor volume was assumed to be 30 μg/g. The main composition and density of the tumor are the same as with the brain tissue. The epithermal neutron beam from the Massachusetts Institute of Technology research reactor was used as the neutron source where the detailed spectrum information can be found (Mirzaei et al., 2014). The distance between the neutron source and the center of the tumor was set at 30 cm (Raaijmakers et al., 1997). The size of the neutron source was set at a 4 cm diameter to match the size of the tumor. The diagram modeled in Geant4 is shown in Fig. 11. The results were tabulated in Table 1. For the target (tumor) dose of 1 Gy, the number of detected 0.478 gamma ray was 4.43×10^7, with the overall detection efficiency of approximately 0.154% when the distance of the scatter detector to the skin was 5 cm. The result was lower than the earlier estimate, which can be explained by the attenuation and the different source volume (i.e., 4 cm diameter). With the increasing distance of the scatter detector to the skin, the overall detection efficiency decreased, as shown in Fig. 12.

4. Conclusions

In this study, an optimized Compton camera in a parallel configuration was investigated to measure the emitted prompt gamma rays during BNCT. With the calculated result and reasonable and practical considerations, the dimensions of the optimized Compton camera are 10 cm lateral width of the two detectors with a thickness of 3 cm and 10 cm for the scatter detector and absorber detector, respectively. The distance between the two detectors is 1 cm. The optimized configuration was based on the optimal detection efficiency of single Compton interactions (for the scatter detector) and of true events (for the absorber detector and the distance between two detectors). The overall detection efficiency of the optimized Compton camera for
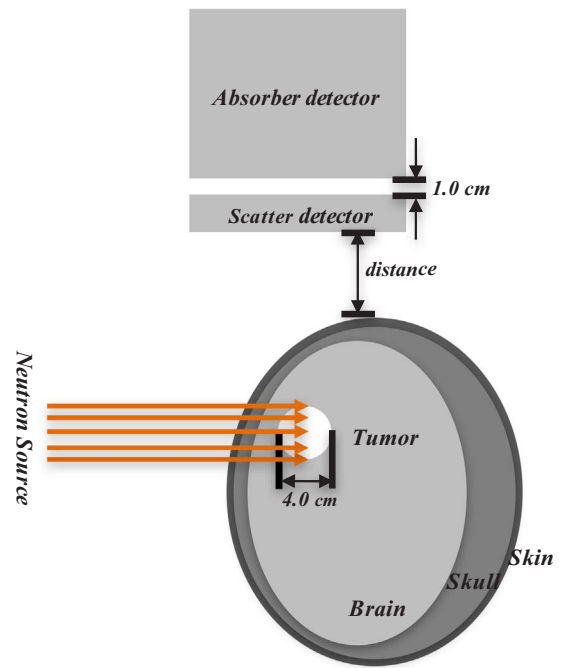

Fig. 11. The diagram modeled in Geant4 with Snyder's head phantom.

Table 1
Overall detection efficiency of the prompt gamma rays with the optimized Compton camera in a BNCT situation with 30 ppm ^{10}B concentration in the tumor region when the distance of the scatter detector to the skin was 5 cm.

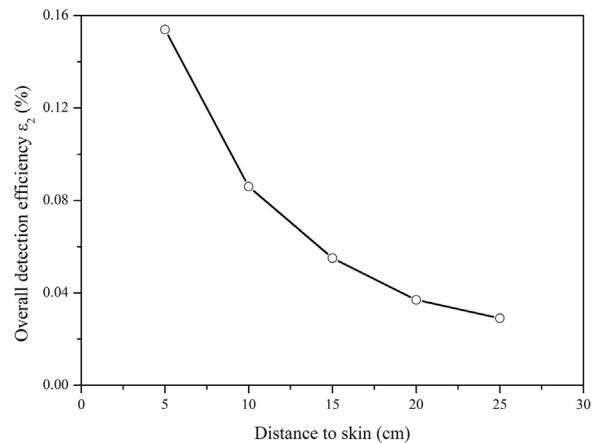| Category	Value
0.478 MeV Gamma generated in the tumor region	2.88×10^{10} per Gy
Detected in the Compton camera	4.43×10^7 per Gy
Overall detection efficiency (Compton camera)	0.154%

Fig. 12. Overall detection efficiency of the optimized Compton camera with different distances to the head of the patient.

the isotropic gamma source was 0.59%. The Snyder's head phantom with a tumor was used to illustrate the flexibility of the optimized Compton camera. Resultantly, the overall detection efficiency was approximately 0.1425%, whereas the sphere tumor was 4 cm in diameter and ~ 1 cm in depth. Therefore, the results of this study provide sound estimates of achievable measurement efficiency under the effects of the thicknesses and lateral widths of the two detectors and the distance between the two detectors. Referring to the previous studies, which include reconstructed images, for Compton Cameras in proton radiotherapy and other applications (Stothers et al., 2016;

Poitrasson-Rivière et al., 2015), our result shows comparable and improved efficiency, which proves the justifiability of the work.

Overall, the goal of this present work only focused on the optimization of the size of the two detectors. The factors arising from the physical (e.g., shielding, contamination, signal process) and reconstruction algorithms were excluded. These factors are expected to decrease the overall detection efficiency, which was optimized in this study; thus, the result must also hold true with other complex conditions. Moreover, only silicon and germanium were considered as the materials for the scatter and absorber detectors in this study. The reason that silicon was chosen as the scatter detector is the potential for electron track Compton imaging (Thirolf et al., 2016), and germanium was chosen for its good energy resolution. Other detector materials must also be explored for the potential improvement of the overall detection efficiency. Future studies should focus on the continued enhancement of the design of the Compton camera, with the long-term goal of developing a clinically viable online imaging of BNCT.

Acknowledgements

References

Bortolussi, S., Ciani, L., Postuma, I., Protti, N., Luca, Reversi, Bruschi, P., Ferrari, C., Cansolino, L., Panza, L., Ristori, S., Altieri, S., 2014. Boron concentration measurements by alpha spectrometry and quantitative neutron autoradiography in cells and tissues treated with different boronated formulations and administration protocols. Appl. Radiat. Isot. 88, 78–80. http://dx.doi.org/10.1016/j.apradiso.2013.12.001.

Chao, D.-S., Liu, Y.-H., Jiang, S.-H., 2016. Demonstration of the importance of a dedicated neutron beam monitoring system for BNCT facility. Appl. Radiat. Isot. 107, 312–316. http://dx.doi.org/10.1016/j.apradiso.2015.11.015.

Cirrone, G.A.P., Cuttone, G., Di Rosa, F., Pandola, L., Romano, F., Zhang, Q., 2010. Validation of the Geant4 electromagnetic photon cross-sections for elements and compounds. Nucl. Instrum. Meth. A618, 315–322. http://dx.doi.org/10.1016/j.nima.2010.02.112.

Geng, C., Tang, X., Guan, F., Johns, J., Vasudevan, L., Gong, C., Shu, D., Da, Chen, 2016. GEANT4 calculations of neutron dose in radiation protection using a homogeneous phantom and a Chinese hybrid male phantom. Radiat. Prot. Dosim. 168, 433–440. http://dx.doi.org/10.1093/rpd/ncv364.

Guan, F., Peeler, C., Bronk, L., Geng, C., Taleei, R., Randeniya, S., Ge, S., Mirkovic, D., Grosshans, D., Mohan, R., Titt, U., 2015. Analysis of the track- and dose-averaged LET and LET spectra in proton therapy using the geant4 Monte Carlo code. Med. Phys. 42, 6234–6247. http://dx.doi.org/10.1118/1.4932217.

Hales, B., Katabuchi, T., Hayashizaki, N., Terada, K., Igashira, M., Kobayashi, T., 2014. Feasibility study of SPECT system for online dosimetry imaging in boron neutron capture therapy. Appl. Radiat. Isot. 88, 167–170. http://dx.doi.org/10.1016/j.apradiso.2013.11.135.

Hang, S., Tang, X., Shu, D., Liu, Y., Geng, C., Gong, C., Yu, H., Da, Chen, 2016. Monte Carlo study of the beam shaping assembly optimization for providing high epithermal neutron flux for BNCT based on D–T neutron generator. J. Radioanal. Nucl. Chem. 1–10. http://dx.doi.org/10.1007/s10967-016-5001-4.

Ishikawa, M., Kobayashi, T., Kanda, K., 2000. A statistical estimation method for counting of the prompt γ-rays from 10B(n,αγ)7Li reaction by analyzing the energy spectrum. Nucl. Instrum. Methods Phys. Res. Sect. A: Accel., Spectrometers, Detect. Assoc. Equip. 453, 614–620. http://dx.doi.org/10.1016/S0168-9002(00)00464-2.

Kobayashi, T., Sakurai, Y., Ishikawa, M., 2000. A noninvasive dose estimation system for clinical BNCT based on PG-SPECT—Conceptual study and fundamental experiments using HPGe and CdTe semiconductor detectors. Med. Phys. 27, 2124–2132. http://dx.doi.org/10.1118/1.1288243.

Lee, T., Lee, H., Lee, W., 2015. Monitoring the distribution of prompt gamma rays in boron neutron capture therapy using a multiple-scattering Compton camera_ A Monte Carlo simulation study. Nucl. Inst. Methods Phys. Res. A 798, 135–139. http://dx.doi.org/10.1016/j.nima.2015.07.038.

Minsky, D.M., Valda, A.A., Kreiner, A.J., Green, S., Wojnecki, C., Ghani, Z., 2011. First tomographic image of neutron capture rate in a BNCT facility. Appl. Radiat. Isot. 69, 1858–1861. http://dx.doi.org/10.1016/j.apradiso.2011.01.030.

Mirzaei, D., Miri-Hakimabad, H., Rafat-Motavalli, L., 2014. Depth dose evaluation for prostate cancer treatment using boron neutron capture therapy. J. Radioanal. Nucl. Chem. 302, 1095–1101. http://dx.doi.org/10.1007/s10967-014-3397-2.

Murata, I., Mukai, T., Nakamura, S., Miyamaru, H., Kato, I., 2011. Development of a thick CdTe detector for BNCT–SPECT. Appl. Radiat. Isot. 69, 1706–1709. http://dx.doi.org/10.1016/j.apradiso.2011.05.014.

Peterson, S.W., Robertson, D., Polf, J., 2010. Optimizing a three-stage Compton camera for measuring prompt gamma rays emitted during proton radiotherapy. Phys. Med. Biol. 55, 6841–6856. http://dx.doi.org/10.1088/0031-9155/55/22/015.

Poitrasson-Rivière, A., Maestas, B.A., Hamel, M.C., Clarke, S.D., Flaska, M., Pozzi, S.A., Pausch, G., Herbach, C.-M., Gueorguiev, A., Ohmes, M.F., Stein, J., 2015. Monte Carlo investigation of a high-efficiency, two-plane Compton camera for long-range localization of radioactive materials. Prog. Nucl. Energy 81, 127–133. http://dx.doi.org/10.1016/j.pnucene.2015.01.009.

Raaijmakers, C.P.J., Konijnenberg, M.W., Mijnheer, B.J., 1997. Clinical dosimetry of an epithermal neutron beam for neutron capture therapy: dose distributions under reference conditions. Int. J. Radiat. Oncol.*Biol.*Phys. 37, 941–951. http://dx.doi.org/10.1016/S0360-3016(96)00623-2.

Rosenschöld, P.M.A., Minarik, D., Östlund, C., Ljungberg, M., Ceberg, C., 2006. Prompt gamma tomography during BNCT—a feasibility study. J. Instrum. 1. http://dx.doi.org/10.1088/1748-0221/1/05/P05003.

Sauerwein, W.A.G., 2012. Principles and Roots of Neutron Capture Therapy. In: Neutron Capture Therapy. Springer Berlin Heidelberg, Berlin, Heidelberg, pp. 1–16. http://dx.doi.org/10.1007/978-3-642-31334-9_1.

Stockhausen, L.C., 2012. Evaluation of Compton Camera Imaging during Boron Neutron Capture Therapy. University of Liverpool, Liverpool, United Kingdom.

Stothers, L., Hou, X., Tanguay, J., Celler, A., 2016. Optimizing multi-stage CdZnTe Compton camera for real-time proton range determination in proton radiotherapy. J. Nucl. Med. 57 (1946–1946).

Thirolf, P.G., et al., 2016. A Compton camera prototype for prompt gamma medical imaging. EPJ Web Conf. 117, 05005. http://dx.doi.org/10.1051/epjconf/201611705005.

Verbakel, W.F.A.R., Stecher-Rasmussen, F., 2001. On-line reconstruction of low boron concentrations by in vivoγ-ray spectroscopy for BNCT. Phys. Med. Biol. 46, 687–701. http://dx.doi.org/10.1088/0031-9155/46/3/305.

Weidenspointner, G., Batic, M., Hauf, S., Hoff, G., Kuster, M., Pia, M.G., Saracco, P., 2013. Validation of Compton scattering Monte Carlo simulation models, in:. Presented at the 2013 IEEE Nuclear Science Symposium and Medical Imaging Conference (2013 NSS/MIC), IEEE, pp. 1–5. doi:http://dx.doi.org/10.1109/NSSMIC.2013.6829500.

Wright, D.H., 2002. Geant4 - A Simul. Toolkit. http://dx.doi.org/10.2172/799992.

Yoon, D.-K., Jung, J.-Y., Jo Hong, K., Suk Suh, T., 2014. Tomographic image of prompt gamma ray from boron neutron capture therapy: a Monte Carlo simulation study. Appl. Phys. Lett. 104, 083521. http://dx.doi.org/10.1063/1.4867338.